



Origin of photocatalytic activity of W/N-codoped TiO₂: H₂ production and DFT calculation with GGA + U



Jianyu Gong^{a,b,*}, Changzhu Yang^a, Jingdong Zhang^b, Wenhong Pu^{a,*}

^a School of Environmental Science and Engineering, Huazhong University of Science and Technology, Luoyu Road 1037, Wuhan 430074, PR China

^b School of Chemistry and Chemical Engineering, Huazhong University of Science and Technology, Luoyu Road 1037, Wuhan 430074, PR China

ARTICLE INFO

Article history:

Received 24 October 2013

Received in revised form 7 January 2014

Accepted 13 January 2014

Available online 22 January 2014

Keywords:

Photocatalysis

Hydrogen production

N and W codoped TiO₂

First-principle calculation

GGA+U

ABSTRACT

In the present investigation, to improve photocatalytic efficiency, nitrogen-doped titanium (N-TiO₂) and tungsten/nitrogen-codoped titanium (W/N-TiO₂) were prepared by a hydrothermal method and characterized by material analysis and first-principle calculation with generalized gradient approximation (GGA). The highest photocatalytic (PC) efficiency (69%) and TOC removal (32%) for methyl orange were achieved on W0.1%-N1 g-TiO₂ under visible light illumination. Besides, the highest amount of hydrogen produced using W0.1%/N1 g-TiO₂ was 35.2 $\mu\text{mol g}^{-1}$ after 2 h of irradiation by visible light. In our simulation models, the GGA + U approach (where $U=6$ and 4 eV) was used for Ti and W atoms, respectively. Density functional theory (DFT) calculation results revealed that a new bond of N-Ti-O linkages formed inside N-TiO₂ was mainly responsible for the narrowed band gap and visible light adsorption. Meanwhile, the intermediate energy states inside the band gap of W/N-TiO₂ were newly formed and resulted in an internal local polarization field between W and N atoms. Consequently, highly effective separation of photogenerated holes and electrons occurred, which was enabled high-performance photocatalysis.

© 2014 Elsevier B.V. All rights reserved.

1. Introduction

Hydrogen production as a potential fuel alternative simultaneously addresses energy and environmental problems because hydrogen combustion produces only water molecules [1,2]. An urgent demand for clean and reusable energy brought about by the serious global energy crisis has recently elicited related research on hydrogen evolution approaches, particularly in photocatalytic hydrogen production from solar energy by semiconductor nano-materials [3,4].

The widely studied TiO₂ photocatalyst is low cost, non-toxic, and chemically stable. TiO₂ is also used for waste remediation, in solar cells, optoelectronic devices, and water splitting [5–10]. However, the wide band gap of TiO₂ (3.2 eV for anatase TiO₂) hinders its photocatalytic applications. Thus, modification of the band gap of TiO₂ should be lessened so that the absorption edge can be shifted to the visible light region. Doping is one of the promising approaches to accomplish this task [11,12]. However, this strategy can also improve the interfacial charge transfer and lower the

photo generated electrons–holes recombination rate result in poor PC activity [13]. Therefore, at recently, TiO₂ codoped with transition metal and nonmetal such as V/N [14], Fe/N [15], Sn/N [16], and S/N [17] is attracting considerable interest.

Among these materials, nitrogen (N) [18,19] is one of the most used doping nonmetal elements because of its reasonable ionic radius, which is similar to that of O. Based on DFT calculations, the N doping introduces a new energy state in band gap of TiO₂, reducing the photon energy required of the creation of photo generated electron–hole pairs, which is ascribed to N 2p states can effectively merge with O 2p states [20]. Meanwhile, tungsten (W) is considered to be one of the best transition metal elements for improving the photocatalysis (PC) activity of TiO₂ [21]. Due to the high valent value of W⁶⁺, W(VI) acts as electron traps inside the lattice of W doped TiO₂, which prevents the recombination of photo generated electron–hole pairs as well as enlarges the absorption edge of excitation light to visible range [22]. However, for W/N-TiO₂, due to the presence of W and N, the energy states of them will be affected together, resulting in high PC performance of W/N-TiO₂ which might be caused by some special reasons. Therefore, a systematic and comprehensive mechanism, as well as a support mechanism for codoped TiO₂ system, must be identified.

Recently, first-principle calculations were conducted for N or W doped TiO₂. Asahi et al. [23] pointed out that the high PC performance of N-TiO₂ is ascribed to the narrowing of band gap by mixing

* Corresponding authors at: Huazhong University of Science and Technology, School of Environmental Science and Engineering, Luoyu Road 1047, Wuhan 430074, PR China. Tel.: +86 27 87792154/+86 73 12184206; fax: +86 27 87543632.

E-mail address: gong_107@163.com (J. Gong).

O 2p and substitutional N 2p states. Diwald et al. [24] thought that interstitial N species doped in TiO_2 could also narrow the band gap. On the other hand, for W doped TiO_2 , Marquez et al. [25] reported that the short distance W–Ti bond is responsible for the narrowed band gap. However, only few reports discussed the theory of high PC activity of W/N– TiO_2 accompanying with real experiments.

Here in, we present our results on the synthesis of TiO_2 , N– TiO_2 and W/N– TiO_2 prepared by hydro-thermal method. These catalysts were characterized by a serial of equipments. Their photocatalytic properties were conducted by the photo degradation of methyl orange (MO) and the production of H_2 under visible light. GGA+U calculations were conducted to further illustrate the mechanism of PC activity of doped or codoped TiO_2 systems.

2. Experimental

2.1. Reagents

Titanium isopropoxide, sodium tungstate, urea, sodium sulfate (Na_2SO_4), anhydrous ethanol, acetone, hydrochloric acid and MO were obtained from Sinopharm Chemical Reagent Co., Ltd., China. Coumarin was purchased from Sigma-Aldrich. All chemicals were of analytical grade. All solutions were prepared with deionized water.

2.2. Preparation of catalysts

TiO_2 was prepared by hydrothermal method. In brief, about 10 mL of titanium isopropoxide was added into 30 mL of an ethanolic solution under vigorous stirring and then labeled as solution A. About 1 mL of hydrochloric acid and 1 mL of deionized water were added into 10 mL of an ethanol solution, which was labeled as solution B. Then, solution B was slowly added to solution A under vigorous stirring. After 1 h stirring, the mixed solution was transferred to a Teflon-lined autoclave at 110 °C for 12 h. The products were harvested by centrifugation and then washed with deionized water several times to remove dissolvable ionic impurities. Finally, as-prepared catalysts were calcined at 600 °C for 2 h, denoted as TiO_2 . On the other hand, after the solution B added into solution A, and the desired concentration of urea or (and) sodium tungstate was added into the mixed solutions and follows the rest of process similar to produce TiO_2 , the N doped TiO_2 (N– TiO_2) or W/N codoped TiO_2 (W/N– TiO_2) samples were obtained.

2.3. Characterization

(TEM) Sirion 200 FSEM (FEI, The Netherlands) and H-600 PV9100 HRTEM (HITCHI, Japan) were employed for catalysts morphology characterization and crystal lattice, respectively. The phase detection and analysis were conducted on XRD (X'Pert PRO, PANalytical B.V., The Netherlands). XPS analysis was performed on a 5300 ESCA instrument (Perkin-Elmer PHI Co., USA). The UV–visible diffuse reflectance spectra were conducted by a UV–visible spectrophotometer equipped with CARY-50 Probe (USA). The fluorescence spectra were recorded on a RF-5301PC (SHIMADZU, Japan) fluorometer. The total organic carbon was determined by TOC-VCSH analyzer (Shimadzu, Japan).

2.4. Evaluation of photocatalytic activity

The photocatalytic activity of all as-prepared samples was evaluated by degrading methyl orange (MO; 5 mg/L) aqueous solution under 300 W Xe lamps through a UV-cutoff filter (<400 nm) as visible light at ambient temperature. The visible light intensity, measured with a visible-light radiometer (Model: FZ-A, China), was

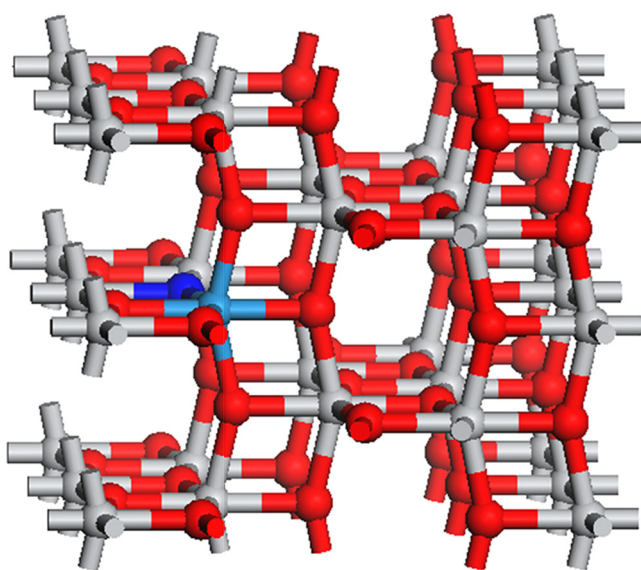


Fig. 1. Additional W and N positions located in the $2 \times 2 \times 1$ anatase supercell for calculations (the colors gray, red, blue and pistachio indicate O, Ti, N and W, respectively). (For interpretation of the references to color in this figure legend, the reader is referred to the web version of this article.)

125 mW cm^{-2} . For the photocatalysis (PC) system, 50 mg of catalyst particle was dispersed in 100 mL of MO aqueous solution. The concentration of MO was analyzed with a UV–visible spectrometer (WFZ UV-2000, China). For absorbance measurement, 3 mL of sample was taken out from the photoreactor at given time intervals after centrifugation. The equipment for PC procedure-based MO degradation was fabricated according to the previous study [26]. The formation of $\cdot\text{OH}$ radicals was monitored by using coumarin as a fluorescence probe. The fluorescence method is a very specific detector with high sensitivity for the quantitative measurement of $\cdot\text{OH}$ radicals, in which coumarin easily reacts with $\cdot\text{OH}$ to form highly fluorescent 7-hydroxy coumarin (umbelliferone) [27]. The absorbance of umbelliferone was recorded based on fluorescence spectra in the absorption range from 400 to 550 nm, using 350 and 455 nm as the excitation and emission wavelengths, respectively.

2.5. The evolution of hydrogen production

The experiments were conducted in an aqueous suspension of catalyst with ethanol as the sacrificial agent under visible light. In brief, photocatalytic hydrogen production reactions were performed in a 50 mL glass reactor. Typically, 50 mg of the catalyst was suspended in 20 mL of H_2O containing 20 mL of ethanol illuminated with visible light. In order to eliminate dissolved oxygen, the suspension was degassed for 30 min with N_2 stream prior to visible light illumination. The amount of H_2 produced was measured by a gas chromatogram (Agilent, 4890D) equipped with a TCD detector.

2.6. Theoretical calculations

All calculations were performed using density functional theory (DFT) based on CASTEP software package within the GGA using Materials Studio v5.5 through a plane-wave pseudopotential approach [28]. The doped systems were constructed from a relaxed anatase TiO_2 supercell ($2 \times 2 \times 1$) containing 48 atoms (16 Ti and 32 O atoms), as shown in Fig. 1. N-doped TiO_2 (N– TiO_2) was modeled by single substitution of N for one O atom per supercell. W/N-codoped TiO_2 replaced one Ti and one O atom per supercell. An ultrasoft pseudopotential was used for geometric optimizations. The electron wave function was expanded in the plane waves up

to a cutoff energy of 400 eV, and a $2 \times 2 \times 1$ Monkhorst–Pack k -point mesh was used to calculate electronic property. Standard local density approximation (LDA + U) was performed to calculate electronic and optical properties on the structures optimized by GGA PBE method [29,30]. To describe Ti 3d states, the LDA + U approach (where $U=6$ and 4 eV, respectively, for Ti and W) was used. The use of U to properly describe the electronic states of d shells was introduced [31]. Mechanical equilibrium was achieved through conjugate gradient minimization of the total energy with a tolerance level of 2×10^{-6} eV, the forces with a tolerance level of 0.05 eV Å $^{-1}$, and the atomic position with a tolerance level of 0.002 Å. The nature of the incorporated N and its loading place in the TiO₂ lattice are still under debate. Here, we chose a reasonable loading place based on another report [32].

3. Results and discussion

3.1. Characterization of catalysts

The shape and lattice of particles were examined by FSEM and HRTEM (Fig. 2). TiO₂ exhibited spherical shape and uniformity in

particles with a large average size of 1 μm (Fig. 2A). The HRTEM image (Fig. 2B) indicated that the lattice spacing was ca. 0.332 nm, corresponding to the (101) facet on TiO₂. After adding N (Fig. 2C), more minute particles were aggregated. The change in morphology may be mainly attributed to urea acting as a surfactant in the thermal treatment, which can inhibit the growth of TiO₂ surface [33]. In the hydrothermal reaction, a semiconducting organic layer may be formed [34], and this layer is chemically bound to TiO₂ because of the surface –OH groups on TiO₂, similar to the case of silica [35]. Reduced particle size is generally beneficial for PC because it leads to quadratic growth of the specific surface area and reactive sites. In addition, the presence of urea enabled the lattice spaces to increase to ca. 0.346 nm (Fig. 2D), indicating that the successful doping of N penetrated the TiO₂ lattice. In the case of W/N-TiO₂ particles, the morphology was similar to that of N-TiO₂, as shown in Fig. 2E. However, the morphology obtained a higher value of lattice space (ca. 0.364 nm) (Fig. 2F), which may be due to the addition of W resulting in the formation of an O–W–N bond. Given the presence of a new bond, the bond lengths and angles between Ti–O, O–Ti–O, or Ti–O–Ti bonds inside W/N-TiO₂ may be affected compare with TiO₂, indicating high PC performance. This topic is discussed later.

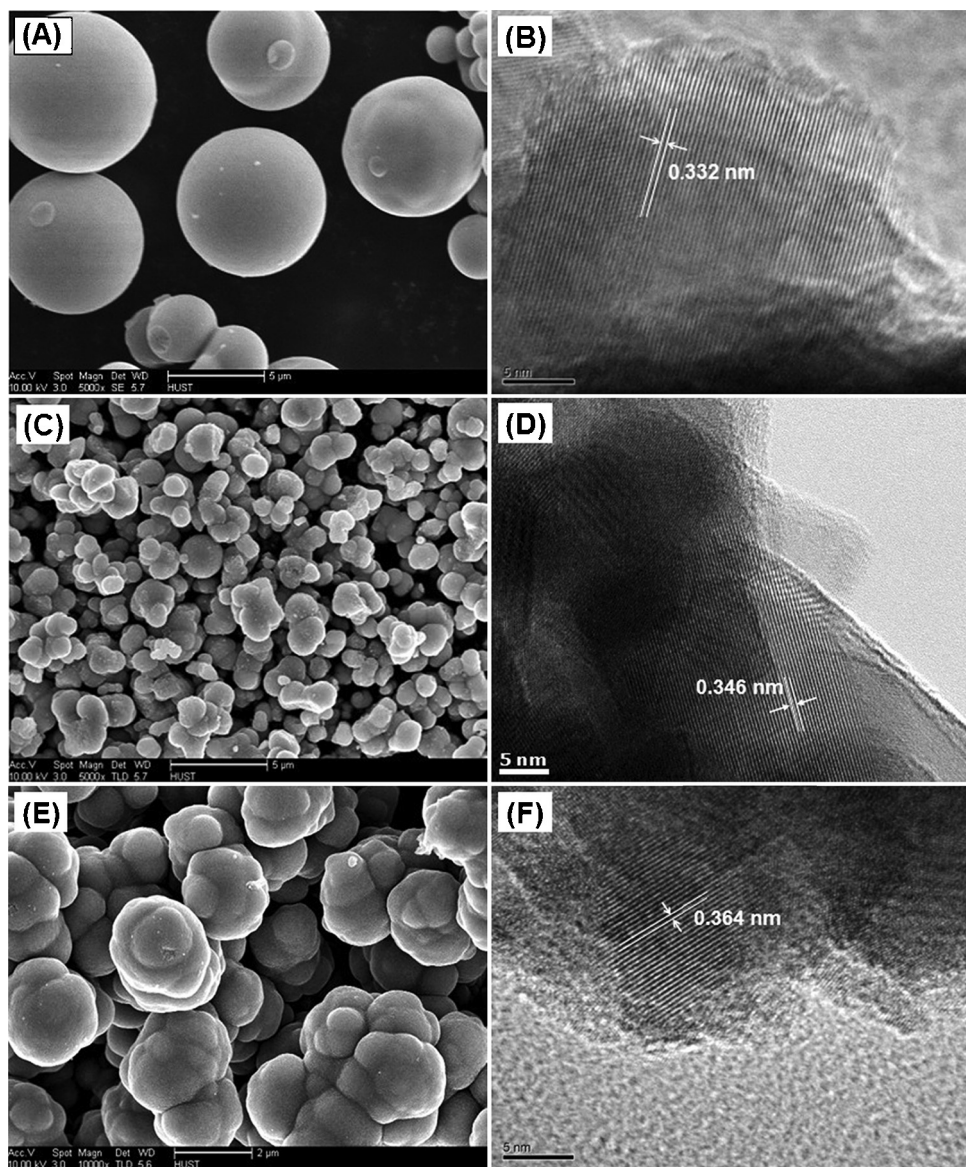


Fig. 2. FSEM images of (A) TiO₂, (C) N1 g-TiO₂, and (E) W0.1%-N1 g-TiO₂ particles. HRTEM images of (B) TiO₂, (D) N1 g-TiO₂, and (F) W0.1%-N1 g-TiO₂ particles.

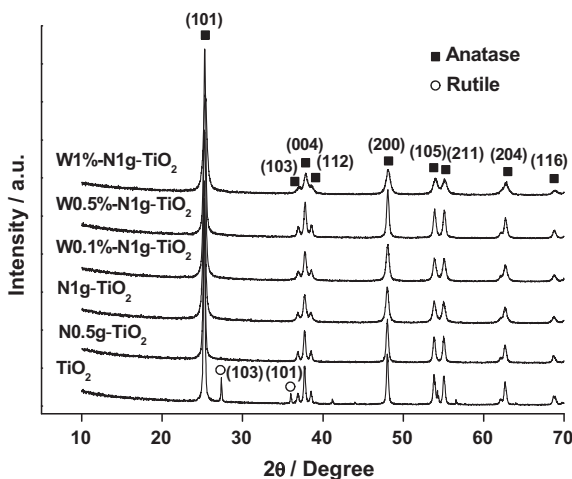


Fig. 3. XRD patterns of catalysts calcined at 600 °C.

Fig. 3 shows the crystal phase of different catalysts. The XRD peaks at $2\theta=27.4$ (R 103) and 36.1 (R 101) are the characteristic peaks of the rutile crystal phase [36] that appear in TiO_2 . The other peaks of samples can be readily indexed to pure anatase phase, consistent with the reported values (JCPDS no. 21-1272). Notably, no visible peaks corresponding to N or W were found after doping, except those of the anatase phase. Thus, the dopant was added into the TiO_2 lattice. According to the Scherrer equation

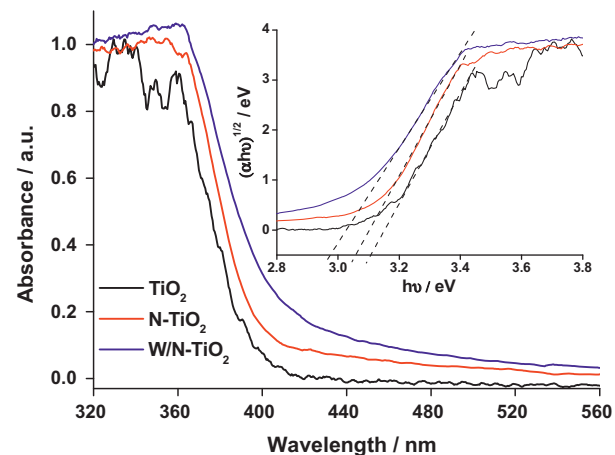


Fig. 4. UV-visible diffuse reflectance spectra of TiO_2 , N1g-TiO_2 and W0.1\%-N1g-TiO_2 . The inset shows the plots of $[\alpha h\nu]^{1/2}$ versus $h\nu$ for band-gap energies.

[37], the average crystalline sizes of these catalysts can be calculated from the major diffraction peak (101) of the anatase phase, as listed in Table 1. The crystalline sizes of TiO_2 , N0.5g-TiO_2 , and N1g-TiO_2 were 22.6, 20.8, and 20.1 nm, respectively. Hence, a large amount of N doping can slightly suppress the growth of TiO_2 . By contrast, the crystalline sizes of W/N-codoped samples were larger than those of pure TiO_2 and N-TiO_2 , indicating that the doping of W can remarkably improve the growth of TiO_2 . Based on Bragg's

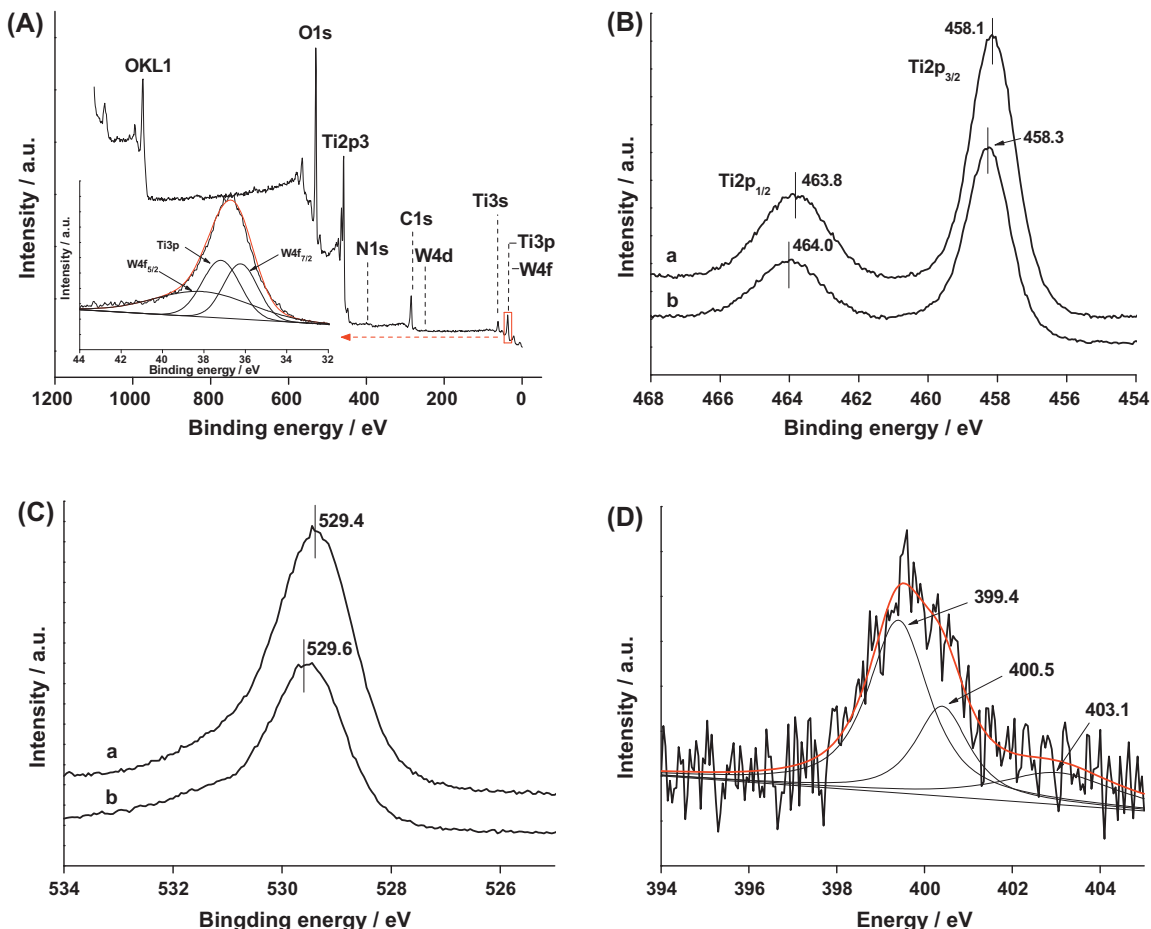


Fig. 5. (A) XPS global spectra of W/N-TiO_2 , and the inset of (A) is the XPS spectra of W 4f. XPS spectra of (B) Ti 2p and (C) O 1s peaks, as well as of (a) TiO_2 and (b) W/N-TiO_2 , respectively. (D) XPS spectra of N 1s peak of W/N-TiO_2 .

Table 1
Physical characteristics of catalysts.

Sample	Crystallite size (nm)	Lattice parameter (Å)	
		<i>a</i> = <i>b</i>	<i>c</i>
TiO ₂	22.6	3.7725	9.5178
N0.5 g–TiO ₂	20.8	3.7622	9.5332
N1 g–TiO ₂	20.1	3.7643	9.5378
W0.1%–N1 g–TiO ₂	25.3	3.7622	9.6223
W0.5%–N1 g–TiO ₂	26.5	3.7642	9.6321
W1%–N1 g–TiO ₂	26.9	3.7702	9.6331

law ($2d_{hkl} \sin\theta = n\lambda$) [38] and the formula for a tetragonal unit cell ($l/(d_{hkl})^2 = (h^2 + k^2)/a^2 + l^2/c^2$), the lattice parameters were calculated and are listed in Table 1. The lattice values along the *c*-axis increased with W doping, indicating that the doped W ion may be present in a hexed-oxidation state, which can partially replace Ti⁴⁺ to form a Ti–O–W bond [39]. Several similar phenomena have been reported in metal doping systems [40,41].

The optical properties of materials were altered after metal doping [42]. Fig. 4 compares the UV–visible absorption spectra of TiO₂, N–TiO₂ and W/N–TiO₂. The inset in Fig. 4 shows the plot of $(\alpha h\nu)^{1/2}$ versus $h\nu$. The vertical segment of the spectra is extended to intersect the $h\nu$ axis (x-axis) to obtain the band gap (E_g) values of catalysts. Afterwards, the diffusive reflectance measurements were converted into the equivalent absorption coefficient by the Kubellka–Munk [43] function as follows:

$$ah\nu = C(h\nu - E_g)^2 \quad (1)$$

$$h\nu = \frac{1240}{\lambda} \quad (2)$$

where α is optical absorption coefficient near the absorption edge for indirect interband transitions, which can be replaced with the absorbance of diffuse reflectance UV–visible, C is the absorption constant for an indirect transition ($C = 1$), $h\nu$ is the photon energy, λ is the wavelength (nm), and E_g is the bandgap energy (eV). The band gap of TiO₂ (3.16 eV) is narrowed to 3.04 and 2.96 eV for N–TiO₂ and W/N–TiO₂, respectively. In the case of N–TiO₂, a visible light absorption shoulder ranging from 380 to 440 nm was obtained from the interstice because of the introduction of new localized states close to the VB edge [44]. Meanwhile, for several kinds of transition metal elements, the cation with d^{10} electronic configurations can introduce occupied d or s states into the VB. Hybridization of these d/s states with O 2p states contributes to an upshift of the top VB and narrows the band gap. Therefore, in the case of W/N–TiO₂, continuous adjustment of the ratios of N 2p states to O 2p states in the VB and W 4d to Ti 4d states in the conduction band (CB) refabricate optimal band structures resulting in the narrowest band gap.

To evaluate the chemical composition and bonding states among elements, XPS was carried out, and the global range XPS spectra are shown (Fig. 5). The main peaks of Ti, O, W and N can be detected. The inset in Fig. 5A is the XPS spectra of W 4f containing Ti 3p. The peak that came out at 36.7 can be attributed to the presence of W 4f_{7/2} and W 4f_{5/2} located at 36.2 and 38.1 eV, respectively. Meanwhile, the other peak at 37.1 eV resulted from the Ti 3p state [45]. Fig. 5B shows that the Ti-2p_{3/2} and Ti-2p_{1/2} peaks of TiO₂ were at 458.1 and 463.8 eV, respectively. However, the peaks for W/N–TiO₂ shifted to a higher binding energy at 458.3 and 464.0 eV for Ti-2p_{3/2} and Ti-2p_{1/2}, respectively. The peak shift indicated that the formation of Ti–N and/or Ti–O–W bands were mainly due to the partial replacement of O and Ti in TiO₂ by N and W, respectively [46]. Fig. 5C shows that the O 1s peak of TiO₂ shifted from 529.4 to 529.6 eV compared with those of W/N–TiO₂. The shift can also be attributed to the substitution of O²⁻ by N³⁻ in the TiO₂ crystal and the formation of new O–Ti–N bond types [47]. Fig. 5D shows a broad peak extending from 397 to 404 eV for

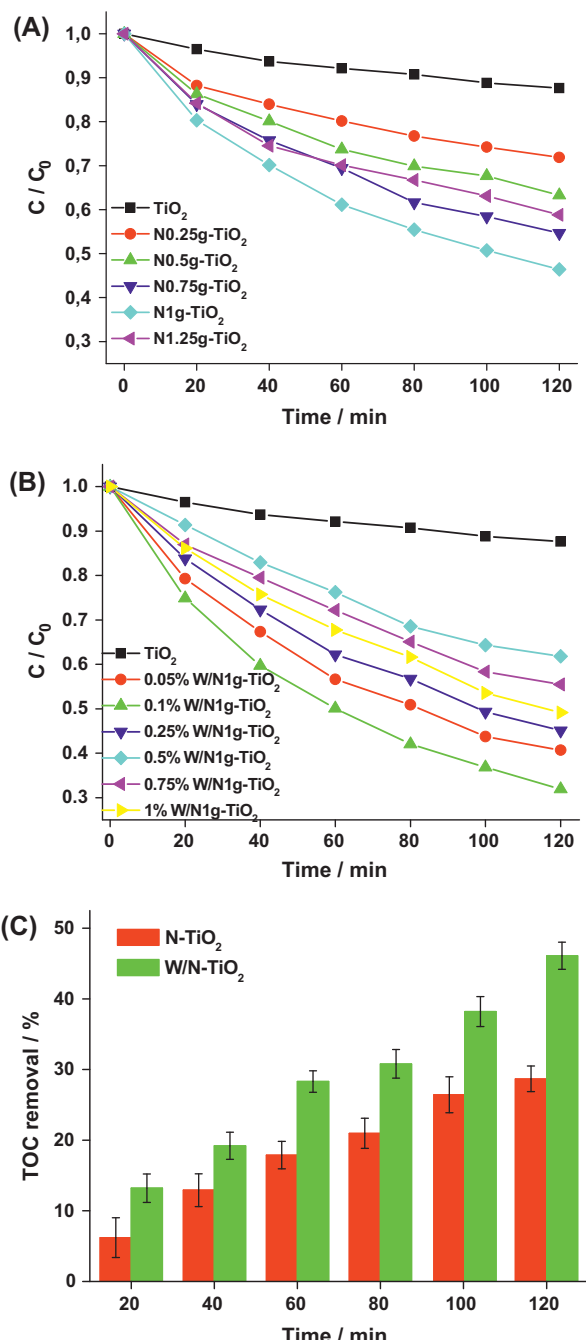


Fig. 6. PC degradation efficiency on (A) N–TiO₂ and (B) W/N–TiO₂. (C) TOC removal of MO by N1 g–TiO₂ and W0.1%–N1 g–TiO₂.

W/N–TiO₂. This peak was fitted using soft XPS peak fit to three very distinct peaks at 399.4, 400.5, and 403.1 eV. The peak at 399.4 eV can be attributed to the substitution of anionic N³⁻ in O–Ti–N linkages [48]. The second peak (400.5 eV) may be due to O–Ti–N linkage or some surface oxidation linkages resulting in the high PC activity of N–TiO₂ [49]. The third peak located at 403.1 eV can be attributed to chemisorbed N-containing species [50].

3.2. Photocatalytic activity of catalysts

The PC activities of samples were first evaluated by the degradation of MO under visible light, as shown in Fig. 6. Fig. 6A shows increased PC efficiency of MO with increased N concentration. N1 g–TiO₂ achieves the best PC efficiency at 55%, which

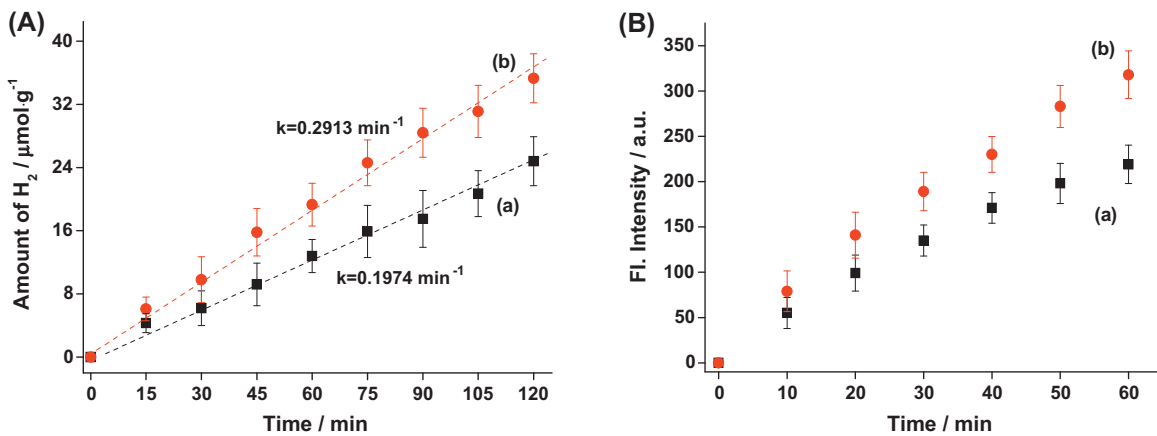


Fig. 7. (A) Time course of H_2 evolution and (B) fluorescence spectra of umbelliferone in 1 mM coumarin solution in the presence of (a) N1 g-TiO₂ and (b) W0.1%-N1 g-TiO₂, respectively.

is almost four times higher than that of TiO₂ (13%). However, with 1.25 g of N, the PC efficiency decreased to 42%. An appropriate amount of impurity (N) inside the lattice of TiO₂ formed a new internal energy level to separate photogenerated holes and electrons. However, too much dopants doped on TiO₂ would accumulate on the interstice or vacancy of lattice to formed a new recombination center, and it would also largely reduce the exposed surface of catalysts and thereby decrease the chance for the photogenerated holes to oxidize pollutant [51]. Thus, 1 g of N was deemed the best concentration to conduct future research. For different W/N-TiO₂ samples (Fig. 6B), the highest PC efficiency (69%) was achieved on W0.1%-N1 g-TiO₂. Besides, the high PC activity of W0.1%-N1 g-TiO₂ was also proven by TOC removal (32%), which was two times higher than that of N1 g-TiO₂ (15%), as shown in Fig. 6C. Similarly, too much of W in codoped samples resulted in lower PC efficiency because the new hole-electron recombination centers will catch the photo generated holes.

PC H_2 evolution experiments were conducted to further understand catalytic ability of samples. Fig. 7A shows the quantity of H_2 evolution with various catalysts as a function of time course through visible light irradiation. The lifetime of photo-induced electron holes can be improved with reagents reacting irreversibly with photo-induced holes or photogenerated oxygen. Thus, the hydrogen evolution rate increased because of the reactions between photogenerated electrons and water [52,53]. W0.1%-N1 g-TiO₂ comprised 35.1 $\mu\text{mol g}^{-1}$ H_2 after 2 h of irradiation, which was much higher than that of N1 g-TiO₂ (24.8 $\mu\text{mol g}^{-1}$). A higher

hydrogen production rate of 0.2913 $\mu\text{mol min}^{-1}$ was also obtained from W0.1%-N1 g-TiO₂, which was almost 1.47 times that of N1 g-TiO₂ (0.1974 $\mu\text{mol min}^{-1}$). Conversely, almost no H_2 evolution was detected from TiO₂ even after 2 h of irradiation (not shown).

The PC activity of samples was further confirmed by the detection of $\bullet\text{OH}$ radicals. Fig. 7B shows changes in the PL spectra of umbelliferone generated in 0.1 mM coumarin solution by visible light irradiation as a function of irradiation time. The PL intensity was directly related to the amount of $\bullet\text{OH}$ radicals [54]. The PL intensity produced by W0.1%-N1 g-TiO₂ was much higher than that of N1 g-TiO₂ indicating that the former had the highest PC activity, which well agreed with PC results. Meanwhile, weak PL intensity was observed for the TiO₂ because it was not activated by visible light (not shown).

3.3. Analysis of DFT calculations

GGA + U can partially correct the band gap relative to experimental value and is usually used to deal with a strongly correlated system [55]. Generally, the main effect of U is to change the location of the impurity energy state inside band gap. However, the relative energies among possible positions of electron localization remain unchanged while different U values are used [56]. So, we thus focus on results using a U value of 6 eV. The relationship between the band gap of TiO₂ and value of U (on Ti-d) was calculated and is shown in Fig. 8A. The inset in Fig. 8A is the band gap of TiO₂ (2.45 eV), and the U value is 6 eV. The density of state (DOS) of catalysts was

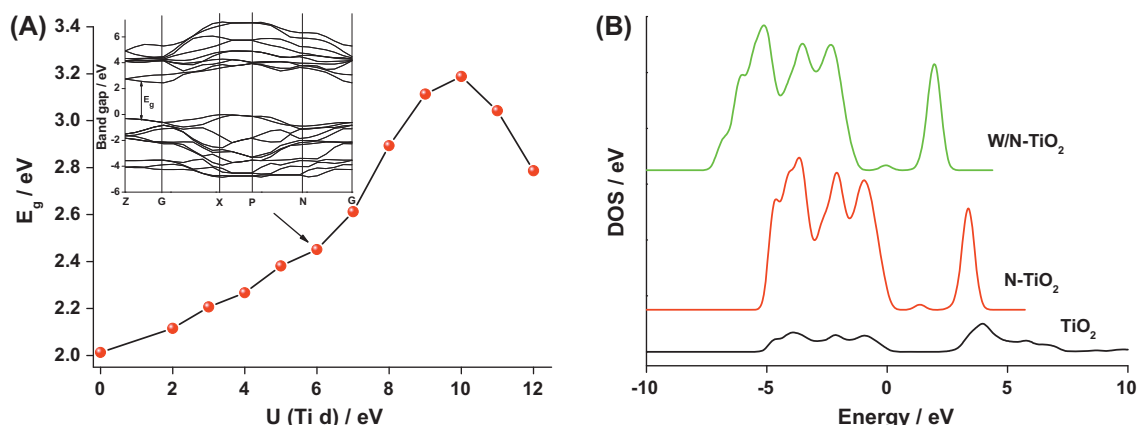


Fig. 8. Band gaps (E_g) of TiO₂ calculated based on different U (Ti-d state) parameters within the LDA + U program. The inset is the band gap of TiO₂, and U (Ti-d state) = 6.

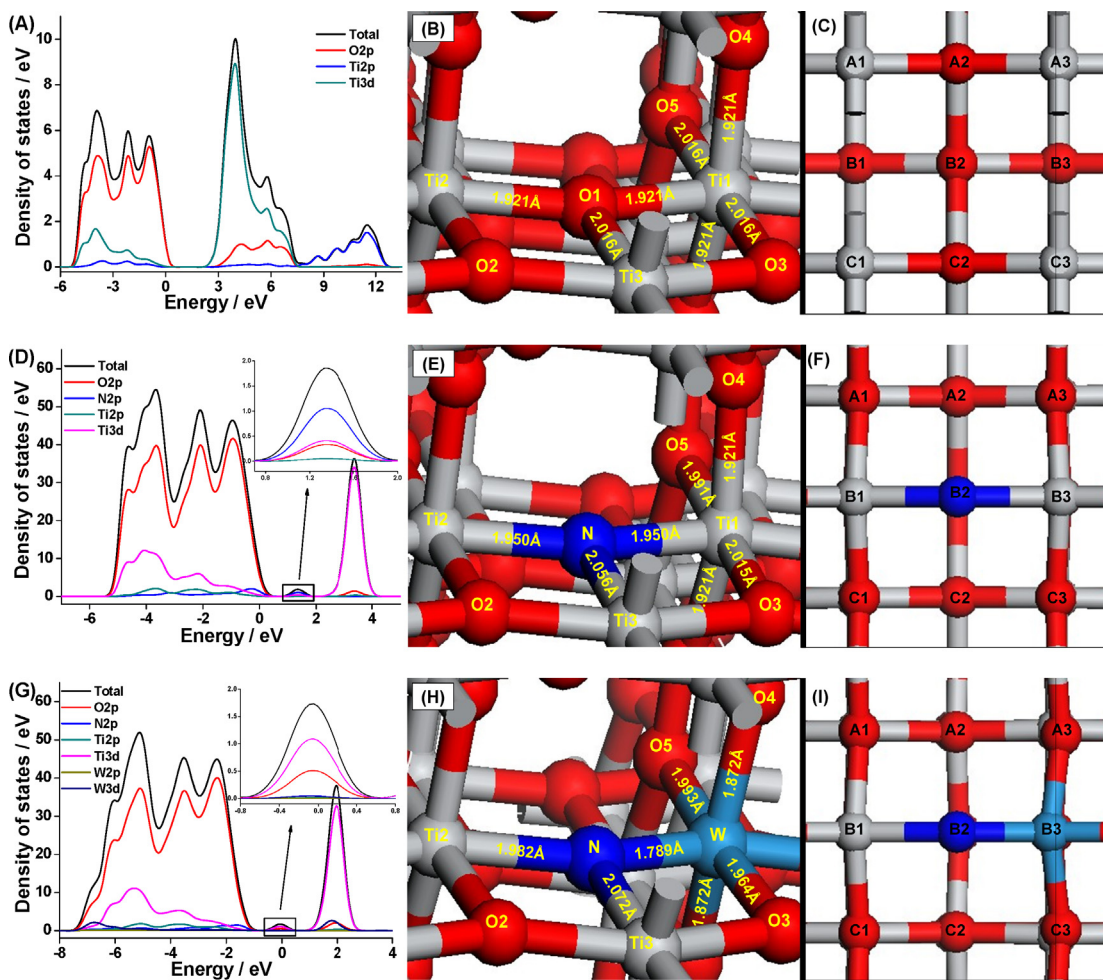


Fig. 9. PDOS of (A) TiO_2 , (D) N-TiO_2 and (G) W/N-TiO_2 . Structure around the dopant site for (B) TiO_2 , (E) N-TiO_2 and (H) W/N-TiO_2 . Atomic structure (showing only one plane) for (C) TiO_2 , (F) N-TiO_2 and (I) W/N-TiO_2 . The colors gray, red, blue and pistachio denote O, Ti, N and W, respectively. The position of atoms is also marked with numbers.

calculated to compare the modifications in electronic structure of the different doped systems, as shown in Fig. 8B. The band gap of TiO_2 was found to be nearly ca. 2.2 to 2.5 eV [55], which was much smaller than the experimental value because of the shortcomings of the exchange–correction function in describing excited states [57,58]. Fig. 8B shows that the calculated band gap of TiO_2 , N-TiO_2 and W/N-TiO_2 were 2.45, 1.56 and 1.14 eV, respectively. Interestingly, for N-TiO_2 , the internal energy level came out, resulting from charge hybridization between N 2p, O 2p and Ti 3p (as proven later). Cheng et al. [44] pointed out that interstitial N-TiO_2 result in a visible light absorption shoulder from 380 to 500 nm because of the introduction of localized states near the VB edge. Under irradiation, photogenerated electrons can easily transfer from the VB to intermediate states, and electrons in the newly formed states can subsequently transit to the CB when excited [59]. These phenomena are responsible for the visible light-excited PC activity of N-TiO_2 . Similarly, for W/N-TiO_2 , another state is located inside the band gap of W/N-TiO_2 , which is mainly contributed by the hybridization of electrons between Ti 3p and O 2p. Generally, these intermediate energy levels pave the way for high PC performance [60]. To clearly understand what happened inside these lattices, projected DOS (PDOS) and bond length were calculated.

The PDOS of catalysts are shown in Fig. 9. The PDOS in Fig. 9A revealed that for TiO_2 , the O 2p states dominate the top VB, and the Ti 3d states dominate the bottom of the CB. After the addition of N in N-TiO_2 (Fig. 9D), O atoms still occupied the VB. However, a new

interior energy state was observed in the middle of the band gap mainly dominated by N 2p states (inset of Fig. 9D). Thus, the state is localized in the band gap, resulting in the narrowing of the maximum band value compared with undoped TiO_2 . Considering that the atomic radius of N was slightly larger than that of O, N-TiO_2 at the vacant oxygen position resulted in the distortion of octahedral TiO_4 units [61]. Therefore, the strong orbital interaction between N and neighboring O atoms in an octahedral unit led to the separation of $[\text{Ti } 3\text{d} + \text{O}_2 \text{ p}\pi]$ hybrid states [62]. Consequently, vicinal Ti and O atoms simultaneously interacted and partly overlapped with electron orbits, resulting in changes in bond length and bond angle. Fig. 9B and E shows the geometry around the dopant site in anatase for TiO_2 and N-TiO_2 , respectively. The N-Ti1 bond distance of N-TiO_2 (1.950 Å) increased compared with that of O1-Ti1 in the case of TiO_2 (1.921 Å). Meanwhile, the transformation of bond length changed bond angles. Fig. 9C and F shows that O-Ti-N, which is mainly responsible for absorption in the visible region of N-TiO_2 [23,62], caused the bond angle of N-TiO₂ ($\angle \text{A3B3B2}$) to be narrowed to 89.38° compared with that of O-Ti-O (90°).

In the case of W/N-TiO_2 , the PDOS is shown in Fig. 9G. The top VB and bottom CB are still governed by O 2p and Ti 3d, respectively. However, the VB edge shifted from 0.38 to -0.98 eV because of the presence of W, which drastically affected the Ti unoccupied DOS and subsequently influenced Ti–N bonds. The CB edge also moved from 2.37 to 0.96 eV [63]. In addition, the newly formed intermediate energy state was not mainly charged by N 2p, as shown in the

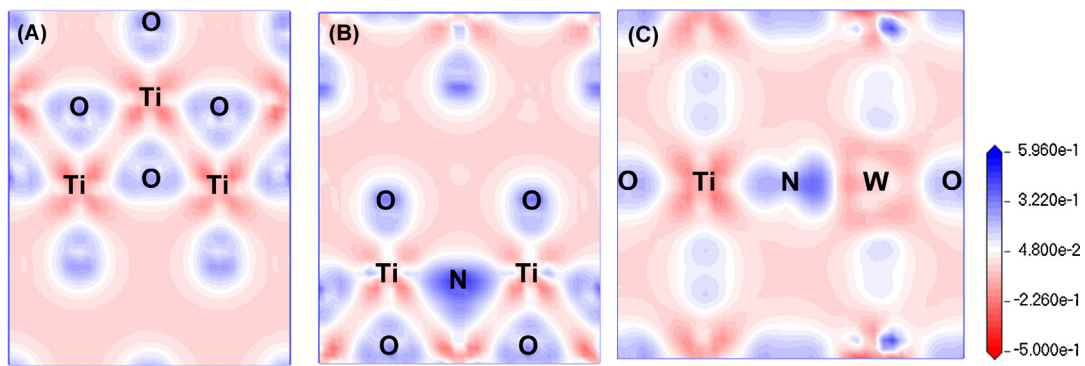


Fig. 10. Electron density differences among (A) TiO_2 , (B) N-TiO_2 and (C) W/N-TiO_2 (showing only one plane).

inset of Fig. 9G. The presence of W inside the lattice of W/N-TiO_2 affected the intermediate energy state, in which the physically larger atomic size of W occupied more volume than Ti, resulting in the distortion of Ti–N bond. The distortion of the Ti–N bond was proven by the reconstruction of the W/N-TiO_2 lattice, in which the bond length and bond angle changed (Fig. 9H and I). The bond distance of W–N decreased to 1.789 Å, which was much shorter than that of N–Ti (1.950 Å) for N-TiO_2 . Consequently, a strong W–N bond formed in W/N-TiO_2 , resulting in increased bond angle of O–W–N ($\angle \text{O}4\text{WN}$) (98.97°).

To further understand the transfer mechanism of electrons, electron density difference maps of TiO_2 , N-TiO_2 and W/N-TiO_2 were obtained, as shown in Fig. 10. Fig. 10B shows that in the case of N-TiO_2 , the inclusion of N in the lattice resulted in a paramagnetic impurity and doublet ground state. A strong N 2p character was largely localized on N atom because of the high density of electrons. Fig. 10B also clearly shows electron transfers from Ti to the coordinated N. Therefore, greater charge depletion (accumulation) around Ti (N) can be obtained in N-TiO_2 than in TiO_2 (Fig. 10A), resulting in the distortion of bonds in the lattice of N-TiO_2 .

In W/N-TiO_2 (Fig. 10C), electron density was more localized on N than W atom. A covalent bond formed between W and N atoms, indicating that N formed a stable eight-electron shell with no unpaired electron. Long et al. [64] pointed that the unpaired electron of N inside W/N-TiO_2 forms a new bond with W because of the higher Bader charges [65,66] of W/N-TiO_2 than N-TiO_2 . Charge imbalance between W^{6+} and N^{3-} ions inside the lattice may have occurred, as clearly shown in the surrounding electrons of N atom in Fig. 10C. Consequently, an electric dipole between W and N atoms forms. The dipole moment also causes an internal local polarization field that improves the separation of photogenerated holes and electrons, which plays a key role in photocatalysis [67,68].

4. Conclusions

N-TiO_2 and W/N-TiO_2 nanoparticles were successfully prepared to serve as photocatalysts for the PC degradation of pollutants and hydrogen evolution by an easy hydrothermal process. As expected, the PC efficiency for pollutant degradation increased, and hydrogen evolution with W/N-TiO_2 (0.1 g TiO_2) exhibited improved PC activity. The degradation efficiency of methyl orange increased to 69% on 0.1 g TiO_2 under visible light illumination, which is almost 5.3 and 1.25 times higher than that for TiO_2 and N-TiO_2 (1 g TiO_2), respectively. In addition, the PC rate for hydrogen production increased to 0.2913 min^{-1} after visible light irradiation, which is about 1.48 times higher than that for N-TiO_2 (1 g TiO_2). The high PC efficiency of W/N-TiO_2 can be mainly attributed to the new intermediate states. DFT calculations indicated that the hybridization between N 2p and O 2p led to the formation of intermediate energy responsible for

the high PC activity of N-TiO_2 . Formation of an N–W–O bond and a polarization field between W and N atoms improved the PC activity of W/N-TiO_2 . All calculation results rationalized the experimental observations on enhanced PC activity.

Acknowledgments

This work was supported by the National Natural Science Foundation of China (Grant no. 61172005). The authors thank the Analytical and Testing Center of HUST for the use of SEM and XRD equipments.

References

- [1] A. Kudo, Y. Miseki, Chem. Soc. Rev. 38 (2009) 253–278.
- [2] Q. Xiang, J. Yu, M. Jaroniec, J. Am. Chem. Soc. 134 (2012) 6575–6578.
- [3] Q. Li, B.D. Guo, J.G. Yu, J.R. Ran, B.H. Zhang, H.J. Yan, J.R. Gong, J. Am. Chem. Soc. 133 (2011) 10878–10884.
- [4] M.D. Ye, J.J. Gong, Y.K. Lai, C.J. Lin, Z.Q. Lin, J. Am. Chem. Soc. 134 (2012) 15720–15723.
- [5] K. Nakata, A. Fujishima, J. Photochem. Photobiol. C 13 (2012) 169–189.
- [6] E. Grabowska, J. Reszczynska, A. Zaleska, Water Res. 46 (2012) 5453–5471.
- [7] S.K. Choi, H.S. Yang, J.H. Kim, H. Park, Appl. Catal., B 121–122 (2012) 206–213.
- [8] J.T. Carneiro, C.C. Yang, J.A. Moulijn, G.D. Mul, J. Catal. 277 (2011) 129–133.
- [9] E. Ronca, M. Pastore, L. Belpassi, F. Tarantelli, F.D. Angelis, Energy Environ. Sci. 6 (2013) 183–193.
- [10] S.W. Liu, J.G. Yu, M. Jaroniec, Chem. Mater. 23 (2011) 4085–4093.
- [11] Y.F. Li, D.H. Xu, J.I. Oh, W.Z. Shen, X. Li, Y. Yu, ACS Catal. 2 (2012) 391–398.
- [12] M.V. Dozzi, E.J. Sellis, Photochem. Photobiol., C 14 (2013) 13–28.
- [13] H.R. Zhang, K.Q. Tan, H.W. Zheng, Y.Z. Gu, W.F. Zhang, Mater. Chem. Phys. 125 (2011) 156–160.
- [14] J.W. Liu, R. Han, Y. Zhao, H.T. Wang, W.J. Lu, T.F. Yu, Y.X. Zhang, J. Phys. Chem. C 115 (2011) 4507–4515.
- [15] M.J. Yang, C. Hume, S. Lee, Y.H. Son, J.K. Lee, J. Phys. Chem. C 114 (2010) 15292–15297.
- [16] E.J. Wang, T. He, L.S. Zhao, Y.M. Chen, Y.A. Cao, J. Mater. Chem. 21 (2011) 144–150.
- [17] Q.J. Xiang, J.G. Yu, M. Jaroniec, Phys. Chem. Chem. Phys. 13 (2011) 4853–4861.
- [18] D.D. Camillo, F. Ruggieri, S. Santucci, L. Lozzi, J. Phys. Chem. C 116 (2012) 18427–18431.
- [19] J. Wang, D.N. Tafen, J.P. Lewis, Z.L. Hong, A. Manivannan, M.J. Zhi, M. Li, N.Q. Wu, J. Am. Chem. Soc. 131 (2009) 12290–12297.
- [20] C. Di Valentini, G. Pacchioni, A. Selloni, S. Livraghi, E. Giamello, J. Phys. Chem. B 109 (2005) 11414–11419.
- [21] E.M. Neville, M.J. Mattle, D. Loughrey, B. Rajesh, M. Rahman, J.M. Don MacElroy, J.A. Sullivan, K. Ravindranathan Thampi, J. Phys. Chem. C 116 (2012) 16511–16521.
- [22] T. Tatsuma, S. Saitoh, Y. Ohko, A. Fujishima, Chem. Mater. 13 (2001) 2838–2842.
- [23] R. Asahi, T. Washizuka, N. Yoshino, K. Aoki, Y. Taga, Science 293 (2001) 269–271.
- [24] O. Divald, T.L. Thompson, T. Zubkov, E.G. Goralski, S.D. Walck, J.T. Yates Jr., J. Phys. Chem. B 108 (2004) 6004–6008.
- [25] A.M. Marquez, J.J. Plata, Y. Ortega, J.F.J. Sanz, Phys. Chem. C 115 (2011) 16970–16976.
- [26] J.Y. Gong, W.H. Pu, C.Z. Yang, J.D. Zhang, Chem. Eng. J. 209 (2012) 94–101.
- [27] H.M. Guan, L.H. Zhu, H.H. Zhou, H.Q. Tang, Anal. Chim. Acta 608 (2008) 73–78.
- [28] Z.G. Wu, R.E. Cohen, Phys. Rev. B 73 (2006), 235116–234122.
- [29] V.I. Anisimov, J. Zaanen, O.K. Andersen, Phys. Rev. B: Condens. Matter 44 (1991) 943–954.
- [30] J.P. Perdew, K. Burke, M. Ernzerhof, Phys. Rev. Lett. 77 (1996) 3865–3868.
- [31] B.J. Morgan, G.W. Watson, J. Phys. Chem. C 114 (2010) 2321–2328.

[32] M.E. Kurtoglu, T. Longenbach, K. Sohlberg, Y. Gogotsi, *J. Phys. Chem. C* 115 (2011) 17392–17399.

[33] S. Sakulkhaemaruethai, T. Sreethawong, *Int. J. Hydrogen Energy* 36 (2011) 6553–6559.

[34] D. Mitoraj, H. Kisch, *Chem. Eur. J.* 16 (2010) 261–269.

[35] A. Schmidt, *Chem. Ing. Tech.* 38 (1966) 1140–1144.

[36] L.Q. Jing, B.F. Xin, F.L. Yuan, L.P. Xue, B.Q. Wang, H.G. Fu, *J. Phys. Chem. B* 110 (2006) 17860–17867.

[37] J. Wang, Y.K. Zhou, Y.Y. Hu, R. O'Hayre, Z.P. Shao, *J. Phys. Chem. C* 115 (2011) 2529–2536.

[38] N. Lu, X. Quan, J.Y. Li, S. Chen, H.T. Yu, G.H. Chen, *J. Phys. Chem. C* 111 (2007) 11836–11842.

[39] J.R. Stromberg, J.D. Wnuk, R.A.F. Pinlac, G.J. Meyer, *Nano Lett.* 6 (2006) 1284–1286.

[40] S. Bagwasi, B.Z. Tian, J.L. Zhang, M. Nasir, *Chem. Eng. J.* 217 (2013) 108–118.

[41] J.F. Zhu, Z.G. Deng, F. Chen, J.L. Zhang, H.J. Chen, M. Anpo, J.Z. Huang, L.Z. Zhang, *Appl. Catal. B* 62 (2006) 329–335.

[42] M.H. Zhou, J.G. Yu, J. Hazard. Mater. 152 (2008) 1229–1236.

[43] J.Y. Gong, C.Z. Yang, W.H. Pu, J.D. Zhang, *Chem. Eng. J.* 167 (2011) 190–197.

[44] X.B. Cheng, C. Burda, *J. Am. Chem. Soc.* 130 (2008) 5018–5019.

[45] X. Zhang, F. Liu, Q.L. Huang, G. Zhou, Z.S. Wang, *J. Phys. Chem. C* 115 (2011) 12665–12671.

[46] X. Chen, C. Burda, *J. Phys. Chem. B* 108 (2004) 15446–15449.

[47] G. Sauthier, E. György, A. Figueras, R.S. Sánchez, J. Hernando, *J. Phys. Chem. C* 116 (2012) 14534–14540.

[48] T.C. Jagadale, S.P. Takale, R.S. Sonawane, H.M. Joshi, S.I. Patil, B.B. Kale, *J. Phys. Chem. C* 112 (2008) 14595–14602.

[49] S.S. Thind, G.S. Wu, A.C. Chen, *Appl. Catal., B* 111–112 (2012) 38–45.

[50] X.X. Yang, C.D. Cao, L. Erickson, K. Hohn, R. Maghirang, K. Klabunde, *Appl. Catal., B* 91 (2009) 657–662.

[51] Y.F. Wang, M.C. Hsieh, J.F. Lee, C.M. Yang, *Appl. Catal., B* 142–143 (2013) 626–632.

[52] N.D. Feng, Q. Wang, A.M. Zheng, Z.F. Zhang, J. Fan, S.B. Liu, *J. Am. Chem. Soc.* 135 (2013) 1607–1616.

[53] S. Ardo, Y.L. Sun, A. Staniszewski, F.N. Castellano, G.J. Meyer, *J. Am. Chem. Soc.* 132 (2010) 6696–6709.

[54] J. Zhang, Y. Nosaka, *J. Phys. Chem. C* 117 (2013) 1383–1391.

[55] R. Long, Y. Dai, G. Meng, B.B. Huang, *Phys. Chem. Chem. Phys.* 11 (2009) 8165–8172.

[56] N.A. Deskins, R. Rousseau, M. Dupuis, *J. Phys. Chem. C* 115 (2011) 7562–7572.

[57] J.G. Yu, Q.J. Xiang, M.H. Zhou, *Appl. Catal., B* 90 (2009) 595–602.

[58] J.B. Lu, Y. Dai, H. Jin, B.B. Huang, *Phys. Chem. Chem. Phys.* 13 (2011) 18063–18068.

[59] Q.J. Xiang, J.G. Yu, M. Jaroniec, *Phys. Chem. Chem. Phys.* 13 (2011) 4853–4861.

[60] X.G. Ma, Y. Wu, Y.H. Lu, J. Xu, Y.J. Wang, Y.F. Zhu, *J. Phys. Chem. C* 115 (2011) 16963–16969.

[61] Z.Z. Zhang, X.X. Wang, J.L. Long, Q. Gu, Z.X. Ding, X.Z. Fu, *J. Catal.* 276 (2010) 201–214.

[62] F. Spadavecchia, G. Cappelletti, S. Ardizzone, M. Ceotto, L. Falciola, *J. Phys. Chem. C* 115 (2011) 6381–6391.

[63] M. Fernández-García, A. Martínez-Arias, A. Fuerte, J.C. Conesa, *J. Phys. Chem. B* 109 (2005) 6075–6083.

[64] R. Long, N. English, *J. Appl. Phys. Lett.* 94 (2009) 132102–132104.

[65] G. Henkelman, A. Arnaldsson, H. Jónsson, *Comput. Mater. Sci.* 36 (2006) 354–360.

[66] E. Sanville, S.D. Kenny, R. Smith, G. Henkelman, *J. Comput. Chem.* 28 (2007) 899–908.

[67] M.C. Long, W. Cai, Z.P. Wang, G. Liu, *Chem. Phys. Lett.* 420 (2006) 71–76.

[68] Y. Inoue, *Energy Environ. Sci.* 2 (2009) 364–386.